A prototype model for evaluating SKA-LOW station calibration

A.J.J. van Es*[a], M.G. Labate[a], M.F. Waterson[a], J. Monari[b], P. Bolli[b], D. Davidson[c], R. Wayth[c], M. Sokolowski[c], P. Di Ninni[b], G. Pupillo[b] , G. Macario[b], G. Virone[d], L. Ciorba[d], F. Paonessa[d]

[a]SKA Organisation, Jodrell Bank, Lower Withington, Macclesfield, UK,;
[b]INAF, National Institute for Astrophysics, Italy;
[c]ICRAR-Curtin University, Australia
[d]Consiglio Nazionale delle Ricerche - IEIIT, Turin, Italy

ABSTRACT

The Square Kilometre Array telescope at low-frequency (SKA-Low) will be a phased array telescope supporting a wide range of science cases covering the frequency band 50 - 350 MHz, while at the same time asking for high sensitivity and excellent characteristics. These extremely challenging requirements resulted in a design using 512 groups of 256 log periodic dual polarized antennas each (where each group is called "station"), for a total of 131072 antennas. The 512 stations are randomly distributed mostly within a dense area around the centre of the SKA-Low, and then in 3 arms having 16 station clusters each.

In preparation for the SKA Phase 1 (SKA1) System Critical Design Review (CDR), prototype stations were deployed at the Murchison Radio-astronomy Observatory (MRO) site (Western Australia) near the Murchison Widefield Array (MWA) radio telescope. The project involved multiple parties in an International collaboration building and testing different prototypes of the SKA1-Low station near the actual site. This resulted in both organisational and logistic challenges typical of a deployment of the actual telescope.

The test set-up involved a phased build-up of the complex station of log-periodic antennas, by starting from the deployment of 48 antennas and related station signal processing (called AAVS1.5, where AAVS stands for Aperture Array Verification System), followed by expansion to a full station (AAVS2.0). As reference a station with dipole antennas EDA2 (EDA: Engineering Development Array) was deployed. This test set-up was used for an extensive test and evaluation programme. All test antenna configurations were simulated in detail by electromagnetic (EM) models, and the prediction of the models was further verified by appropriate tests with a drone-based radio frequency source. Astronomical observations on Sun and galaxy transit were performed with calibrated stations of both EDA2, AAVS1.5 and AAVS2.0. All 3 configurations were calibrated. EM modelling and calibration results for the full station AAVS2.0 and EM verification for the AAVS1.5 station are presented.

The comparisons between the behaviour of the log-periodic antennas and the dipoles have advanced our understanding the calibration quality and the technological maturity of the future SKA1-Low array.

Keywords: Radio Astronomy, calibration, aperture arrays, phased arrays

*a.vanes@skatelescope.org, www.skatelescope.org, SKA Organisation

1. INTRODUCTION

1.1 Background

The SKA1, when completed, will be the largest radio telescope in the world and will consist of two telescopes: SKA1-Mid in the Karoo in South Africa and SKA1-Low in the Murchison Desert in Western Australia. The SKA1-Low telescope is a phased array telescope with a baseline of 65 km. The core of the telescope is very dense and contains almost 50% of all the stations. The remaining stations are distributed along 3 quasi spiral arms in 48 clusters of 6 stations (16 clusters in each arm) [2].

The station hardware and array signal processing was designed by the Aperture Array Design & Construction (AADC) Consortium [9] that constructed a first station prototype (AAVS1) using the log-periodic antenna SKALA2.0 [7]. In preparation of the SKA1 System CDR a new prototype was constructed implementing a number of lessons learned from the AAVS1. This new station prototype, AAVS2.0, in line with the most recent SKA1-Low architecture, has the following differences when compared to AAVS1: the centralised architecture is replaced by a distributed approach for distribution of the power and of the receiving analog signal; the RF to optical convertor (Front End Module) is moved from within the antenna assembly to a dedicated power and signal distribution box connecting 16 antennas; the station diameter is increased by approximately 10%; and the SKALA2.0 is replaced by the SKALA4.1. The beamforming hardware (SPS-subsystem) remained identical to AAVS1.

1.2 Purpose of work

The prime objective of the AAVS2.0 prototype model from a hardware and infrastructure point of view was to implement an SKA1-Low station, in order to isolate the characteristics of the station that most affect calibration at the station level.

The experiments conducted at the prototype are supported by an extensive simulation program using EM simulations of the antennas that accurately predict the measured behaviour of the system for supporting the fundamental questions on calibration. The simulations supported the preparation for the measurements performed on site and the analysis of the results.

The test and measurement program for the station prototype is therefore informed by the simulation and analysis activities, utilising the hardware and infrastructure established by the Project, and focused on the highest-level goal of assessing station (beam) calibration.

Whilst the individual technologies that compose a SKA1-Low station have a high level of maturity, the combination of these technologies is innovative and challenging, resulting in a low technological readiness level for the overall design. This aspect was highlighted by the CDR of the LFAA where the panel stated that the mutual coupling (both between antennas within the station and between stations within the array) is a technical risk. The recommendations were to further investigate critical properties and functions of the design:

1) Station-level calibration - determining complex gain and delay for all 256 antennas, and stability across the entire frequency range. Potential use of outrigger antennas or holography has yet to be explored.

2) Beam calibration - forming a delay and sum beam, and understanding the properties of such beam

3) Understanding of embedded element patterns in practice

2 DESCRIPTION OF AAVS2.0: SKA1-LOW FIELD NODE AND SPS

This section provides a short description of the architecture of the SKA1-Low relevant to the AAVS2.0 station prototype a described in more detail in [2].

The SKA1-Low is composed of 512 stations. These are made up of groups of 256 dual-polarized log-periodic antennas distributed over a ground plane having a diameter of about 42 meters. The antennas occupy up to 40 meters (physical occupancy of the antennas) and the maximum distance between the centres of two antennas is 38 meters. The antennas are placed accordingly to a specific randomized layout in order to improve the performance (e.g. in terms of grating lobes) of the overall station. Different random layouts are envisaged for the different 512 stations (or at least a subset of those); however, each layout has to guarantee a corridor of 70 cm to reach each antenna for maintenance purposes.

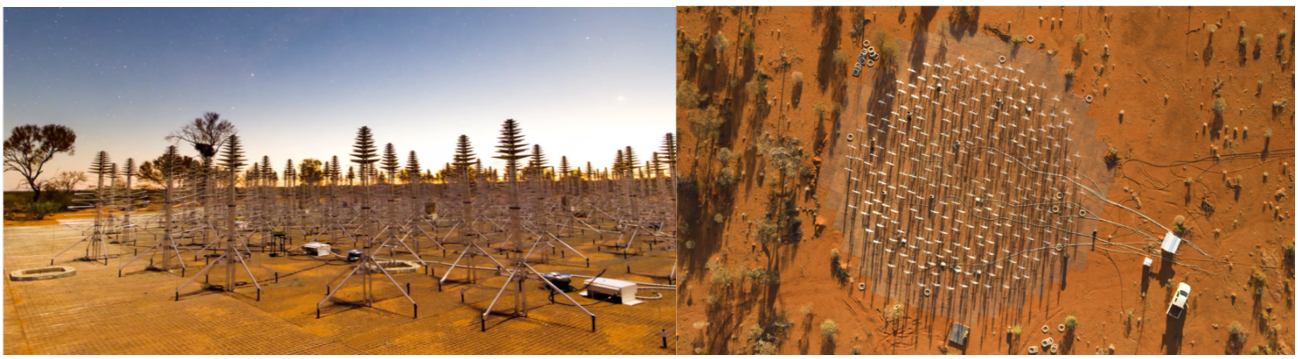

Figure 1: AAVS2.0 station prototype. Left: SKALA4.1 antennas, metallic mesh (ground plane) and SMART boxes. Right: Top view of the AAVS2.0 station, with also the Field Node Distribution Hub (FNDH) (white box) where all the cabling from the SMART boxes for power and signal distribution are connected.

Each antenna consists of the antenna [5] itself and the Low Noise Amplifier (LNA) located at the top of the antenna. The signal from each antenna & LNA is carried through two coaxial cables (one per polarization) to a "Small Modular Aggregation and RFoF Trunk (SMART) Box", where the corresponding Front-End Module (FEM) is located. Each FEM contains an RF amplifier and RF to optical transducer which amplitude-modulates and transmits the two RF signals onto optical fibres corresponding to the two different polarizations (at different optical wavelengths). Sixteen FEMs and a 48V-to-5V power supply are enclosed in a SMART Box, and each SMART Box supports a 'tile' of 16 antennas, so 16 SMART Boxes are needed to serve the 256 antennas.

The 16 SMART Boxes are connected to the FNDH, where mains AC power provided by the main Infrastructure is down converted to 48 V to be distributed to the SMART Boxes. The power is then down converted and redistributed to each antenna via the coaxial cables.

The positioning of each SMART Box is arranged within the ground plane diameter to ensure that the maximum coaxial cable has length of about 10 m or less to avoid standing waves. The location of each SMART Box is determined in response to antenna placement (rather than constraining it).

The analogue signals from each antenna and each polarization arrive at an FNDH where they are aggregated into larger trunk cables (Fibre Cable Assembly – FCA) running to the Central or Remote Processing Facility (CPF/RPFs).

The optical signals are sent from the FNDH to the proper processing facility through a 288-core Fibre Cable Assembly (FCA), which aggregate/breakout fibre-optic infrastructure in order to establish a continuous signal path from each polarization of each antenna to the processing equipment in the facility.

A power control and conversion module, within the FNDH, provides Monitor and Control capabilities via a bidirectional link to the Monitor Control and Calibration System (MCCS) (via the Stations Cabinet Management Board) located in the Central Processing Facility.

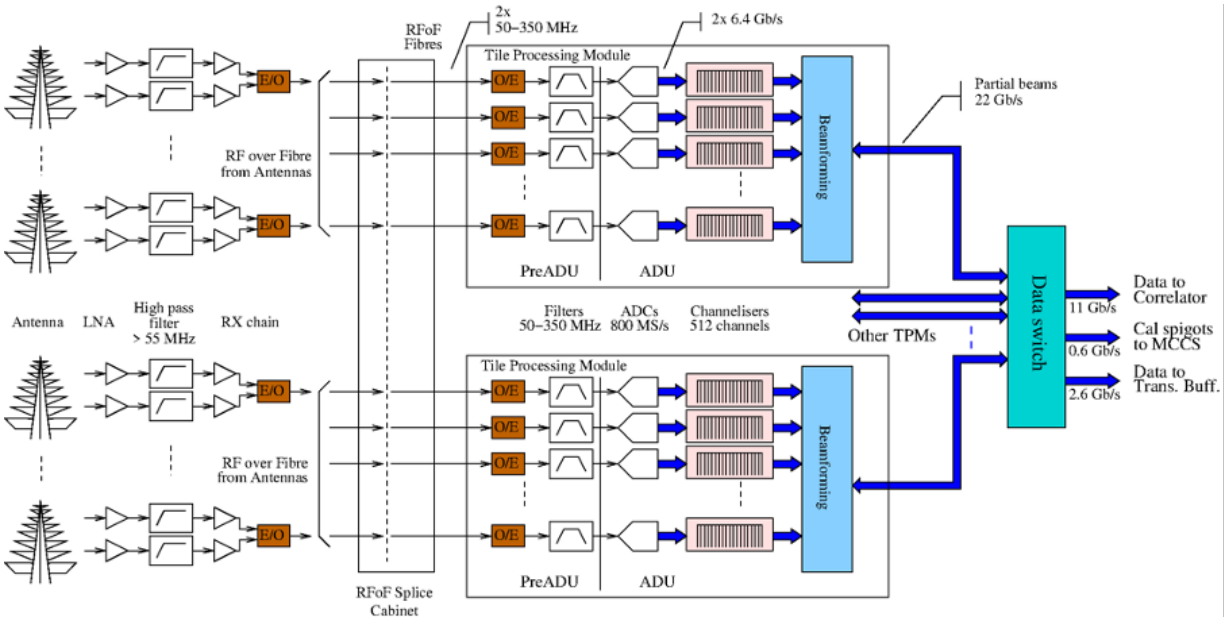

Figure 2: Complete Signal Chain functional diagram

Within the processing facilities, RF signals are carried to individual Tile Processing Modules (TPMs) where the analogue signals are converted back into electrical RF signals and processed. The processing includes filtering, digitization, channelization and beamforming. Each TPM processes 16 dual-polarized antennas (i.e. 32 inputs in total) and forms a partial beam by aligning each signal with respect to the station delay centre, applying the calibration and pointing coefficients to each channel, and summing the signals together. There are 16 TPMs for each station and they are connected in a daisy-chain through a high-speed data switch. The partial beams from each TPM are sent to the next TPM in the chain where the sum of partial beams will happen. The outcome of the overall sum is the station beam. The flexibility of the architecture and the choice of digital beamforming allows generation of multiple station beams as well as sub-station beams (i.e. using a subset of antennas in the station).

Figure 3; The Signal Processing Cabinet and a Tile Processing Module (TPM) on the right

The TPM is composed of two main units: two pre-ADU boards, performing optical to RF conversion and analogue signal conditioning, and the ADU board, performing ADC conversion, digital filtering and signal processing, implemented in a high-speed multilayer digital PCB. The TPMs are part of a Signal Processing System (SPS) which includes cabinets, internal power distribution, water cooling system, clock distribution, SPS network and management system.

The real-time station beamforming [13] is implemented in the firmware executed in the FPGAs inside the TPMs.

Table 1: The main differences between the SKA1 telescope design and the AAVS2.0 prototype.

	SKA1	**AAVS2.0**
Number of stations	512	1
Antenna	SKALA4.1 AL (industrialized version)	SKALA4.1 AL (proto version)
TPM	2xPreADU 2.6 +ADU 1.6 Industrial version Suitable for backplane 2xXilinx 16 nm Kintex Ultrascale XCKU9P 16xADC AD9695 4+4GBy DDR4	2xPreADU 2.1 +ADU 1.2 Proto version 2xXilinx 20 nm Kintex UltraScale XCKU040 16xADC AD9680 4+4GBy DDR3
Subrack	Controlled Subrack Management Board + backplane + power supplies 8xTPM1.6	Passive Subrack with 4xTPM 1.2
Population of the rack	4 Subrack serving 2 stations per rack	2 Subracks serving ½ station per rack
Cooling system	Air cooling of subrack, sealed/integrated heatpipes on TPM	Air cooling
FCA	buried, 2.5km max length	Surface-laid, 5km length
Transient Buffer	Implemented	Not implemented
Monitoring and Control	Integrated with MCCS and Telescope Monitoring and Control (TMC) using TANGO attributes Current and voltage monitoring at antenna-level (implemented in each SMART Box) ON/OFF at antenna level Temperature monitoring within each Smart Box	External command interface (local scripts, webpages) Current and voltage monitoring at the SMART Box (implemented in the FNDH) ON/OFF of half tile (8 antennas) No temperature monitoring

3 AAVS2.0 RESULTS

3.1 AAVS2.0 as part of the SKA-Low program

The SKA-Low is a radio telescope that operates in a relatively new window of the radio astronomy spectrum (50 - 350 MHz) built as an interferometric array. The complexity of the system poses a number of technical challenges that can only be understood by introducing an extensive prototyping effort prior to telescope construction. Complex systems usually employ several prototypes before the start of production. A similar approach is used in SKA-Low:

- Functional prototype (AAVS1.0): where the first design is translated into a hardware realisation. Here the basic design principles are tested and evaluated. To provide input for the next stage of development, this prototype was completed and operational. Outcomes were used for the LFAA design CDR
- Engineering prototypes (AAVS1.5 and AAVS2.0): where lessons of the first prototype are incorporated and manufacturability is investigated. Several iterations of the subsystems are possible. Available results were used for the System CDR.
- Production prototype (AA0.5): the final design for construction as produced by the manufacturers. This design will be subject to a Production Readiness Review. After passing this review the roll out of the SKA-Low telescope stations starts. The build of this prototype will start 18 months after start of construction when the infrastructure for building this small array of 6 stations is ready.

In the following sections, work on the AAVS2.0 is discussed, and some results are presented.

3.2 Test program for the AAVS2.0 prototype

The work on the AAVS2.0 built on the earlier research performed using the AAVS1.0. As the Signal Processing backend and control elements for this program are identical, the only difference between AAVS1.0 and AAVS2.0 is the station front-end (from the antenna up to the processing facility) design and architecture (see also Table 1).

Next to the AAVS2.0 prototype an identical antenna array using MWA (Murchison Widefield Array) dipoles was deployed on advice of the CDR panel for the Low Frequency Aperture Array (LFAA) element. The well-known characteristics of the MWA dipole antennas could serve as a reference for the more complicated structure of the log periodic SKALA type antenna [7]

In order to have a quick start of the program, a simple lay-out of 48 antennas was initially deployed (Figure 4) on site (referred to as AAVS1.5). This simplified lay-out ensured a good understanding of the electromagnetic interaction between the antennas, and interaction represented in so-called ‘embedded element patterns’ (EEP).

The Simulation & Analysis work package is at the core of the project and supported all activities throughout the execution of the observation program. EM models of both antenna types were developed, initially to simulate single antenna beam patterns and subsequently for full station EM simulations.

As the computational effort for the EM simulations is significant (running time for the lower frequencies is in the order of weeks) and the bandwidth of the data capture is also restricted to single frequency channels, seven discrete frequencies for the observations were agreed across the system frequency range: 50, 70, 110, 137, 160, 230 and 320 MHz.

First, detailed full-wave EM simulations of the 48 antennas installed for AAVS1.5 and MWA reference antennas were produced for all 7 discrete frequencies. For a select number of frequencies two independent EM simulation packages FEKO and Galileo IDS [8] were performed to verify the assumptions. These simulations were later experimentally verified using an Unmanned Aerial Vehicle (UAV).

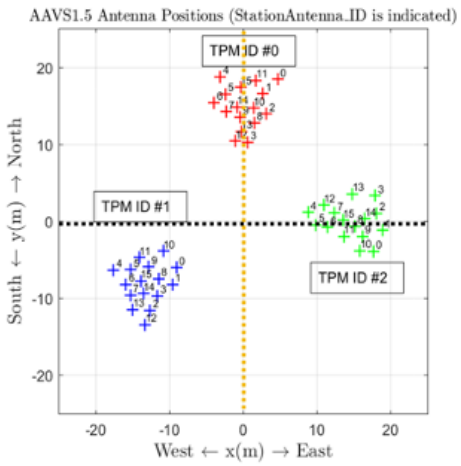

Figure 4: Antennas of AAVS1.5. Dashed lines represent two different scans that compose the overall cross-scan. The yellow/black dashed line corresponds to the quasi-E/H-plane for South-North oriented antennas.

In a second phase the remaining 208 antennas were added resulting in a complete SKA-Low station configuration (referred to as AAVS2.0).

After completing the full station with 256 antennas, the EM simulations were again performed for both antenna types and all frequencies under consideration. This resulted in a complete library allowing derivation of important station performance characteristics such as station sensitivity, station beam characterisation, and station beam polarization properties.

For the AAVS1.5 station lay out (Figure 4) the embedded elements and the beam were verified in the field by using a Unmanned Aerial Vehicle.

Next the intense program of EM simulation and verification of the AAVS properties the the following components at the highest level were tested:

- The calibration of an SKA-Low station to be explored and characterized in detail via direct measurements, including via astronomical tests (using a sky model) and via the use of drones carrying transmitters in both near and far-field;
- Station beamforming this has been demonstrated at AAVS1.0 but further exploration of this is necessary. Work on AAVS2.0 will focus on off-zenith pointings of the beam. To verify performance, the beamforming algorithm will be evaluated against an offline model.
- Station-sensitivity, derived from the EM simulation work and mapped against observational data.
- Polarization properties, exploration of the performance of the full Stokes beams will be performed.
- The consistent collection of ancillary data regarding the costs of the various deployments (in terms of currency units, time, complexity, logistics, etc.).

3.3 Antenna Embedded Element Patterns

Embedded element patterns (EEPs) are the radiation patterns of array elements embedded in the operating array environment. EEPs fully capture mutual coupling, and using appropriate termination on the non-fed array elements, represent the “voltage beams” seen by each element [11].

The EEPs of wide-band antennas operating in highly-coupled electromagnetic environments have been extensively investigated during the development of the LFAA design proposals, and this work has continued under the current program. The primary objective for this effort is to derive and validate EEP which can potentially be used in calibration calculations, and to understand the limitations and errors in these models. The following sections describe electromagnetic modelling of the antenna embedded patterns and the ongoing validation effort to directly measure the antenna patterns in the field using an UAV or drone.

3.4 Numerical simulation of the EEPs

For characterizing the electromagnetic performance of antennas, computer modelling is a well-established field known as 'Computational Electromagnetics': the numerical solution of Maxwell's equations. For modelling the highly-conducting metallic antenna elements of Aperture Arrays, the Method of Moments (MoM) is a very competitive method. A prime consideration when modelling antenna arrays as complex as the AAVS station is to generate a mesh which is sufficiently fine to adequately resolve the current distribution, but no finer, as the computational cost grows very rapidly as the number of mesh elements increases. For electromagnetically large problems, the Fast Multipole Method (FMM) has been adapted to the iterative solution of MoM problems; combined with major advances in high-performance computing, it has proved key to solving very large problems.

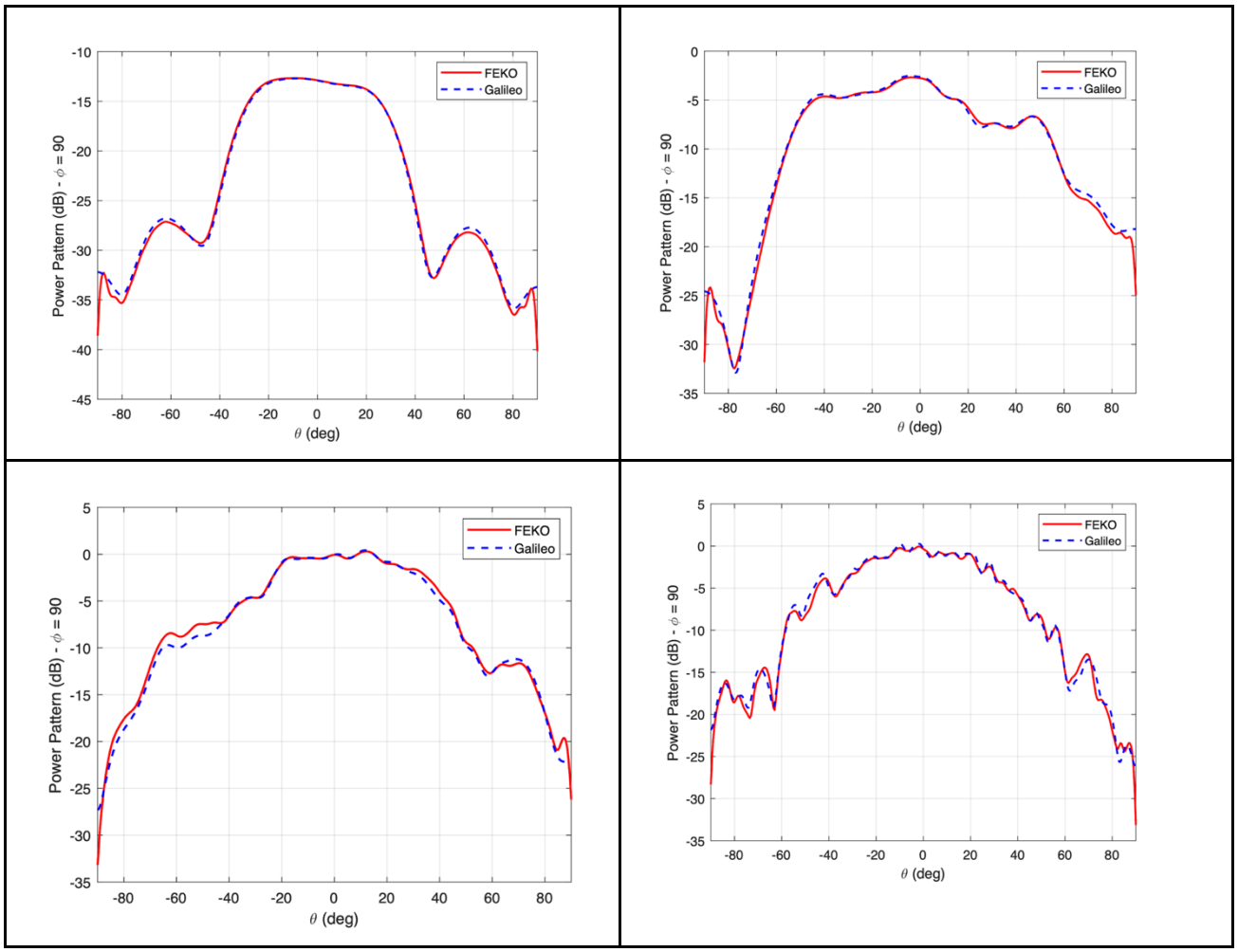

Figure 5: A comparison of EEPs in the E-plane computed using FEKO and Galileo for AAVS2.0. Antenna 100, North-South (Y) pol, 50 MHz, (top left), 80 MHZ (top right); 160 MHZ (bottom left); 350 MHZ (bottom right).

Due to the increased number of dipoles in the SKALA4.1 log-periodic implementation, the SKALA4.1 is appreciably more complex to model numerically than its predecessor in the AAVS1.0, the SKALA2.0, not least in terms of the increased number of solid metal dipoles at the high-frequency end. Two commercial MoM codes have been used: FEKO and Galileo. A comparison of the results obtained for one EEP is shown in Figure 5 for several frequencies for the AAVS2.0. Antenna 100 is located approximately centrally in the station. The results largely show excellent agreement between the codes; both codes use the MoM and make similar assumptions regarding an infinite PEC ground plane, approximating the actual finite wire mesh ground plane. It is notable that most of the patterns are not symmetrical about zenith (θ=0 degrees), despite the central location of this specific element. This is because the EEPs provide a rigorous solution, fully incorporating mutual coupling (unlike the classical array factor method, for instance, which assumes identical element patterns); the quasi-random array configuration of the station results in each element experiencing different mutual coupling levels.

With the full set of embedded element patterns (and depending on EEP termination, possibly the array mutual coupling matrix or scattering matrix which can be computed at the same time), the radiation pattern of the station beam can be computed. Examples are shown in Fig. 6, again comparing FEKO and Galileo simulations. The first sidelobe is at approximately -17dB, consistent with a uniformly illuminated circular aperture. As expected from the quasi-random element distribution, the far-out sidelobe structure is of the order of 1/N in terms of power (approximately -24dB). Some differences in the positions of far-out nulls are visible; these are at very low relative power levels.
Further details are available in [7]for AAVS1.5, and [8] for AAVS2.0.
With the full set of embedded element patterns (and depending on EEP termination, possibly the array mutual coupling matrix or scattering matrix which can be computed at the same time), the radiation pattern of the station beam can be computed. Examples are shown in Fig. 6, again comparing FEKO and Galileo simulations. The first sidelobe is at approximately -17dB, consistent with a uniformly illuminated circular aperture. As expected from the quasi-random element distribution, the far-out sidelobe structure is of the order of 1/N in terms of power (approximately -24dB). Some differences in the positions of far-out nulls are visible; these are at very low relative power levels.
Further details are available in [7]for AAVS1.5, and [8] for AAVS2.0.

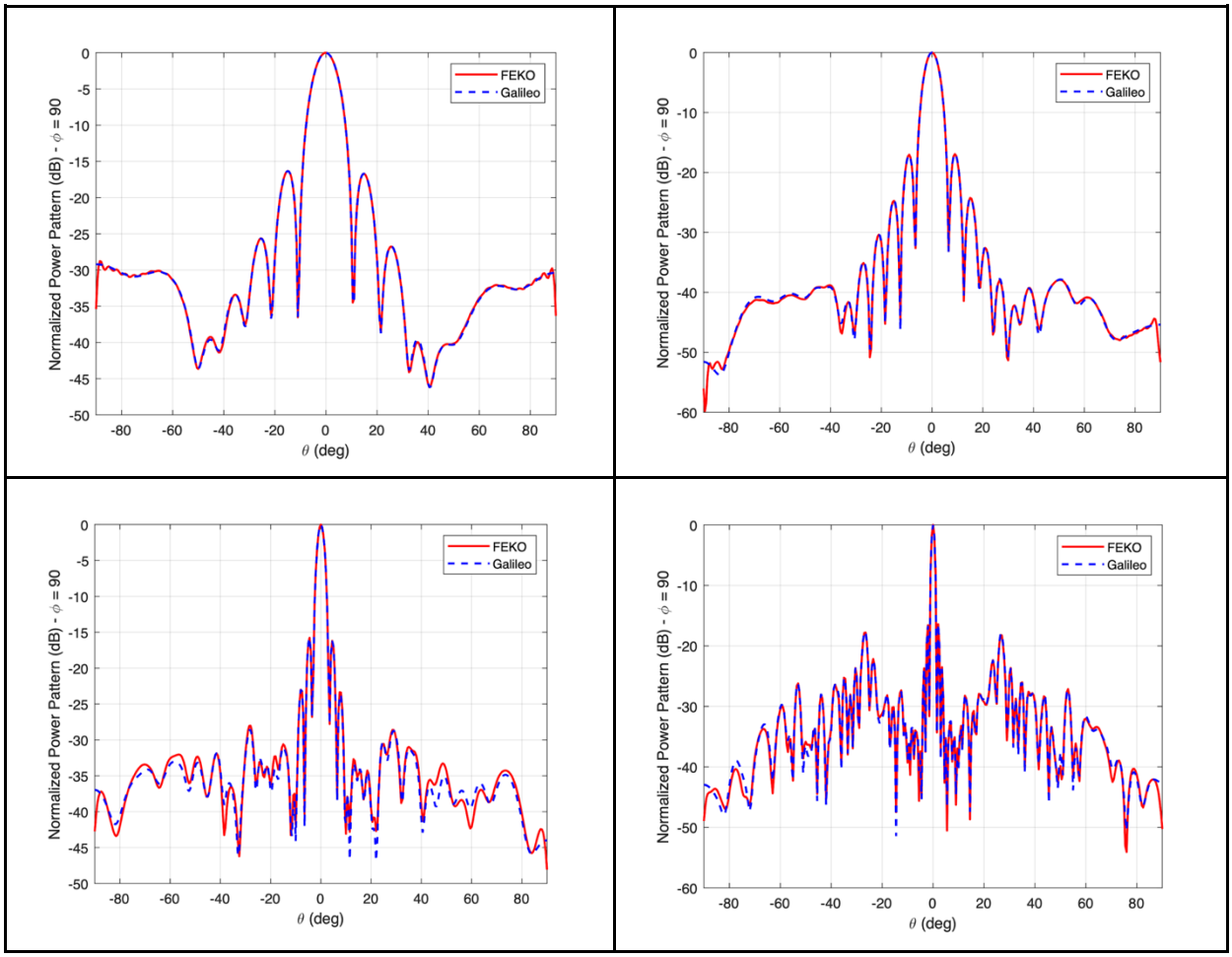

Figure 6: A comparison of zenith-pointing station beams for AAVS2.0, E-plane, NS (Y) pol, synthesized from the EEPs computed by FEKO and Galileo. 50 MHz, (top left), 80 MHZ (top right), 160 MHZ (bottom left); 350 MHZ (bottom right).

3.5 UAV-based Verification of Embedded Element Patterns

Figure shows a micro Unmanned Aerial Vehicle (octocopter) equipped with a radio-frequency synthesizer, a balun and a dipole antenna. Such a system has been already used to characterize isolated antennas [**Error! Bookmark not defined.**][18], small arrays [19]-[21] and large arrays [22]-[24] in terms of both embedded element and array patterns. In 2019, a specific campaign has been conducted at MRO on the AAVS1.5, EDA2 and AAVS1.5 prototypes [25].

Figure 7: Octocopter used at MRO to characterize the station prototypes: the dipole antenna is visible.

An example of measured embedded element patterns (amplitude) is shown in Figure (Figure 8) for two antennas of AAVS1.5 at two different frequencies. It should be noted that the agreement with the simulated results is good i.e. without 0.5-1 dB. A more complete discussion on these results can be found in [25].

Figure 9 instead shows the phase of two embedded element patterns. These data have been derived from differential phase measurements [26] between such elements and a reference antenna selected within the array. It should be noted that the onboard transmitter is not phase-locked to the receiving system located on ground, therefore, an absolute phase measurement is not possible. For this reason, a simulation of the reference antenna has been used in the data processing. Also, in this case, the agreement with the simulations is good.

Finally, Figure 10 shows the array pattern measured on a 16-element subarray of AAVS1.5 at 160 MHz. The array beam has been obtained by summing the acquired complex voltages. The calibration has been performed by equalizing the time series at zenith in both magnitude and phase. The agreement with simulations is remarkable. Other relevant array beams are reported in [25]

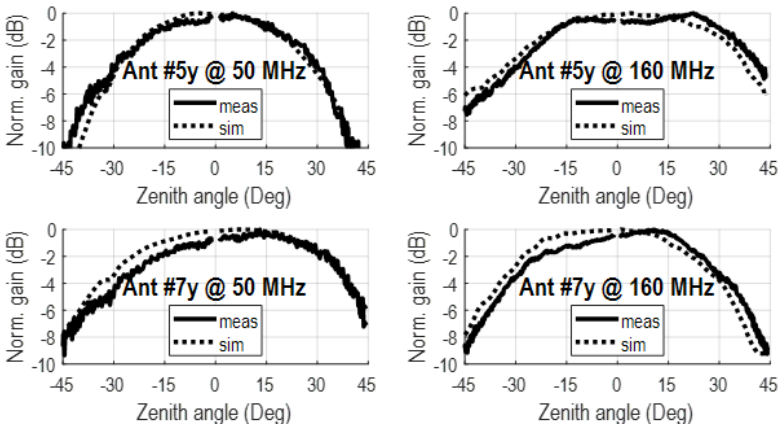

Figure 8: Normalized embedded-element patterns of antenna #5 (upper row) and #7 (lower row) of AAVS1.5 (north-south polarization, cluster #0) at 50 MHz (left column) and 160 MHz (right column).

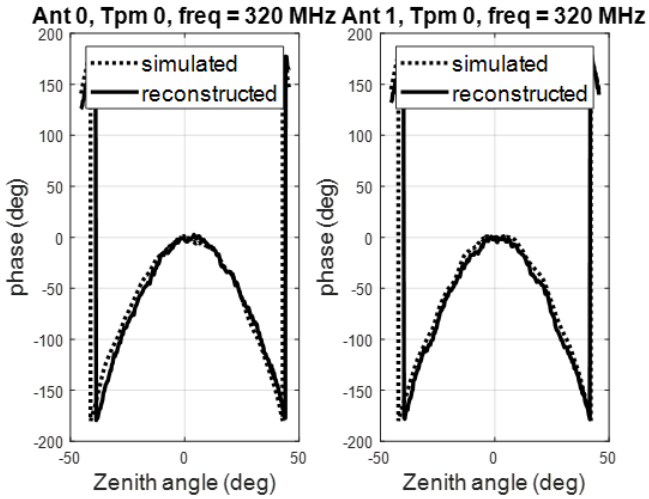

Figure 9: Reconstructed Phase pattern for antenna 1 and 2 of AAVS1.5 at 320 MHz

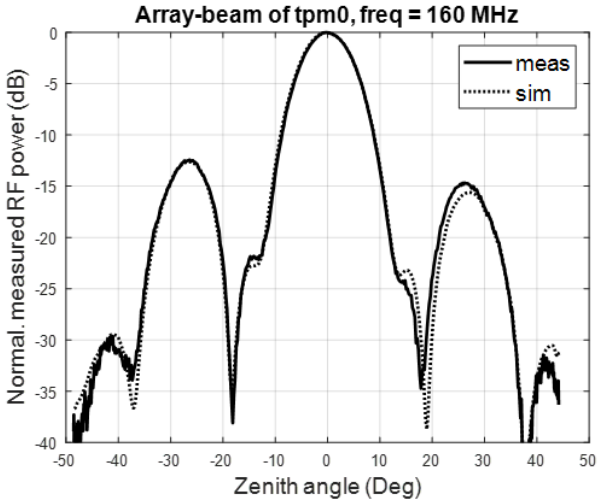

Figure 10: measured and simulated array beam for one tile (16 elements) of AAVS1.5 at 160 MHz.

3.6 Numerical analysis of sensitivity

From an EM point of view, one of the most important requirements for SKA1-Low is the sensitivity, which is the ratio between the effective area and the system noise temperature. The sensitivity thresholds are given by an SKA requirement for the SKA1-Low array at zenith direction.

The sensitivity analysis is computed by using EM commercial software in two different scenarios: first for the isolated antenna (therefore, neglecting mutual coupling among antennas) and then for the full-station case, using the EEPs discussed above. While for the full-station case, the EEPs are summed together, including the geometrical delays, to form the station directivity, for the isolated case we have used the single antenna pattern multiplied by the array factor.

The sensitivity as a function of the spherical coordinates (ϑ,φ) is equal to:

$$Sensitivity(\vartheta,\varphi)=\eta_{Dig}A_{eff}(\vartheta,\varphi)/T_{sys}=\eta_{Dig}[\lambda^2/(4\pi)]G(\vartheta,\varphi)\eta_l/(T_{ant}+(1-\eta_L)290+[T_{LNA}+T_{rx}/G_T])$$

where the station gain ($G(\vartheta,\varphi)$) is given by the station directivity multiplied for the radiation efficiency (η_L). The antenna temperature (T_{ant}), which in principle is the integral of the sky brightness distribution and the antenna pattern, is here simplified to directly the sky noise temperature. Moreover, the T_{LNA} and the G_T terms are respectively the input noise temperature of the LNA and its transducer gain when the amplifier is connected to the real antenna impedance, while the T_{rx} is the noise contribution of the receiving chain after the LNA which is assumed equal to 12000 K (corresponding to 16.3 dB noise figure). Finally, the sensitivity takes into account also the efficiency of the signal processing system (η_{Dig}=0.98%).

The results in terms of sensitivity at zenith in the frequency range 50 to 350 MHz are reported in Figure 11. The blue points indicate the sensitivity computed from the isolated pattern (and therefore without mutual coupling effects); here the frequency resolution is high as the modest EM simulation time requirements for an isolated element permits a large number of frequency points to be computed. The green points give the sensitivity starting from the EEP analyses and therefore with a more rigorous approach. Overall, the agreement between the two sensitivity approaches at zenith is good, which means that the mutual coupling does not impact negatively on the sensitivity. Furthermore, the numerical results show a sensitivity that is always higher than the requirement (red curve). As far as the spectral smoothness is concerned, the ripple in the zenith sensitivity is not always contained within the required envelope (orange dashed curves). Nevertheless, the curvature of the ripple is relatively smooth - and can be readily calibrated out.

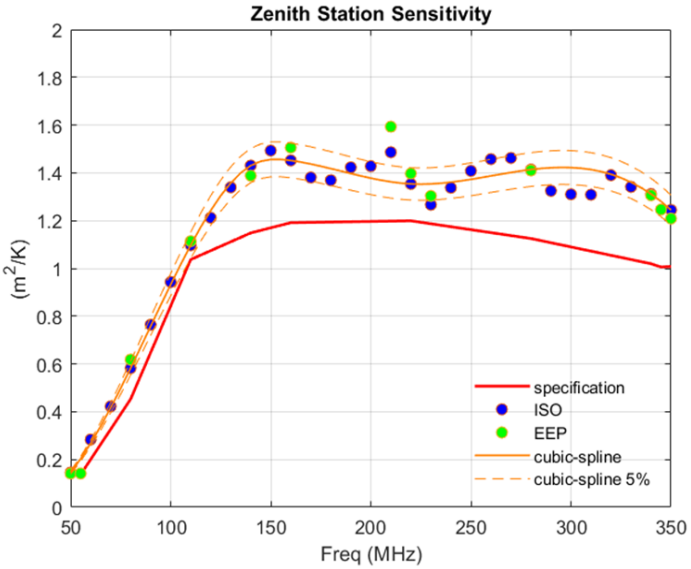

Figure 11: Zenith sensitivity for one station across frequencies computed by using Isolated Element Pattern (blue dots) and Embedded Element Patterns (green dots). The red line is the SKA requirement, while the orange curves are the cubic spline function +/-5%.

3.7 Station Level Calibration

The objective of calibration for an aperture array station is to obtain a set of complex gain terms for each antenna, across the entire frequency band, which permits correction of the signal delay seen at each detector to the actual delay corresponding to the antenna position, and to a nominal, uniform transfer gain for every antenna. Accurate values for these calibration coefficients are necessary to correctly apply the computed pointing delays to each antenna signal, resulting in a coherently summed station beam centered on the desired direction. In a baseband-sampled system such as the AAVS/SKA design, the detector is the ADC sampler, and the subsequent narrow-band poly-phase filter bank allows the measurements to be made in a quasi-monochromatic situation. This enables treating the set of antennas as an interferometer, and therefore use of well-developed radio astronomy tools for self-calibration and imaging to derive the necessary gain coefficients one frequency at a time. This approach relies on knowledge of the input sky signal sufficiently well to generate model interferometric visibilities at the time of the observation, and sufficient system stability to ensure that the signal chain performance does not drift faster than the measurement/computation cadence can follow. The LFAA CDR documentation presented an analysis showing that these conditions could be met in principle, and the primary objective of the AAVS2.0 program is to demonstrate this in practice.

While significant experience and understanding of the calibration problem was obtained during the pre-construction program for the LFAA system, the electromagnetic and mechanical design of the reference design antenna continued to evolve in the lead-up and during the LFAA CDR process. In the lead-up to LFAA CDR, various suites of simulations of station-level performance had been conducted by different groups. While all simulations pointed in the direction of the same risks to calibration, comprehensive cross-checking of the highly complex simulations had not been performed.

Overall, not enough measurement data had been obtained from AAVS1 to explore questions of calibration. Additionally, the antenna design had evolved significantly relative to the AAVS1 system, and the measurements were not underpinned by a verified theoretical understanding of the system.

3.8 Station Calibration Procedure

The station calibration procedure builds upon the techniques described in Benthem et al. (in prep.) but they will be briefly summarised here. The initial bootstrapping process consists of:

- Initial adjustment of signal gain/attenuation such that all antennas have optimal power levels seen at the ADC.
- Confirm the signal mapping from antennas through to digital outputs.
- Solve for complex antenna gains as a function of frequency.
- Solve for the delay for each antenna and polarization.
- Apply the delay solution in the TPMs.

To solve for complex antenna-based gains, the station was used as an interferometer, generating visibilities between all pairs of antennas within the station. Conventional radio astronomy techniques were then used to solve for antenna-based gains. Given the small size of the AAVS1.5 station and the frequency range of interest, the Sun could be used as a dominant unresolved source for most frequencies. In order to ensure correct flux scale of calibration solutions, a flux density model of a quiet Sun was used [27], scaled by the response of a single antenna power pattern at a given frequency, polarization and in the direction of the Sun.

Calibration observations were performed around local midday in order to use the transiting Sun as the calibrator, i.e. observe at its highest elevation where the antenna beam patterns uncertainties are smallest, the antenna polarization leakage is smallest, and the apparent flux density of the sun is largest. Short (2 second) snapshots of correlated data (visibilities) were recorded at each frequency channel (0 - 400 MHz). The data were processed with the MIRIAD data processing suite [16], using the *mfcal* task for phase and amplitude calibration. As part of data processing, the phase center was set at the position of the Sun and a small number of bad antennas were flagged.

Figure 12 shows an example of phase calibration solutions as a function of frequency for 16 antennas of the AAVS1.5 station. It is evident that the phase is a linear function of frequency and, therefore, it could be fitted with a single delay parameter per polarization per antenna. The set of delays fitted to all 512 signal chains (from 256 dual-polarized antennas) was saved to a database. Since these observations were performed regularly (at least once a week) since November 2019, this database enabled monitoring of the stability of calibration solutions over more than a year, which was one of the key deliverables from the arrays.

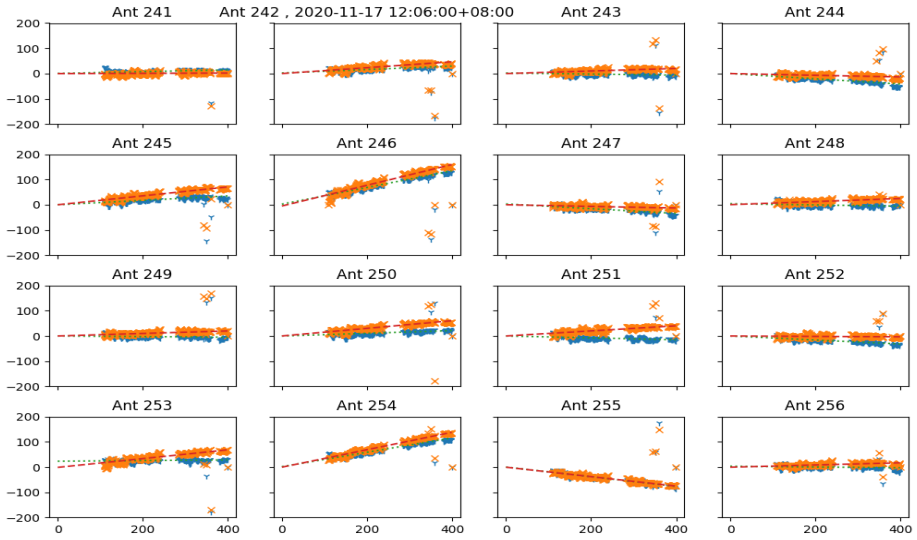

Figure 12:{ Example of phase calibration solutions as a function of frequency plotted for 16 antennas in the AAVS2.0 station. The data were collected around midday on 2020-11-17. Several frequency bands were flagged due to known RFI presence. The phase was fitted with a first order polynomial with an intercept at 0 Hz constrained to be either 0 or 180 degrees. Note that these data were taken after an initial digital delay correction was applied within all TPMs, hence the residual delays (phase slopes) are very small.

Calibration solutions resulting from the solar transit data were then applied to all the data to form all-sky images (see Figure 13) or real-time and off-line station beams collected over the course of the observation (typically 24 hours or more). The single set of calibration solutions was proven to be sufficiently stable to form very good quality all-sky images over time intervals of even up to a few days.

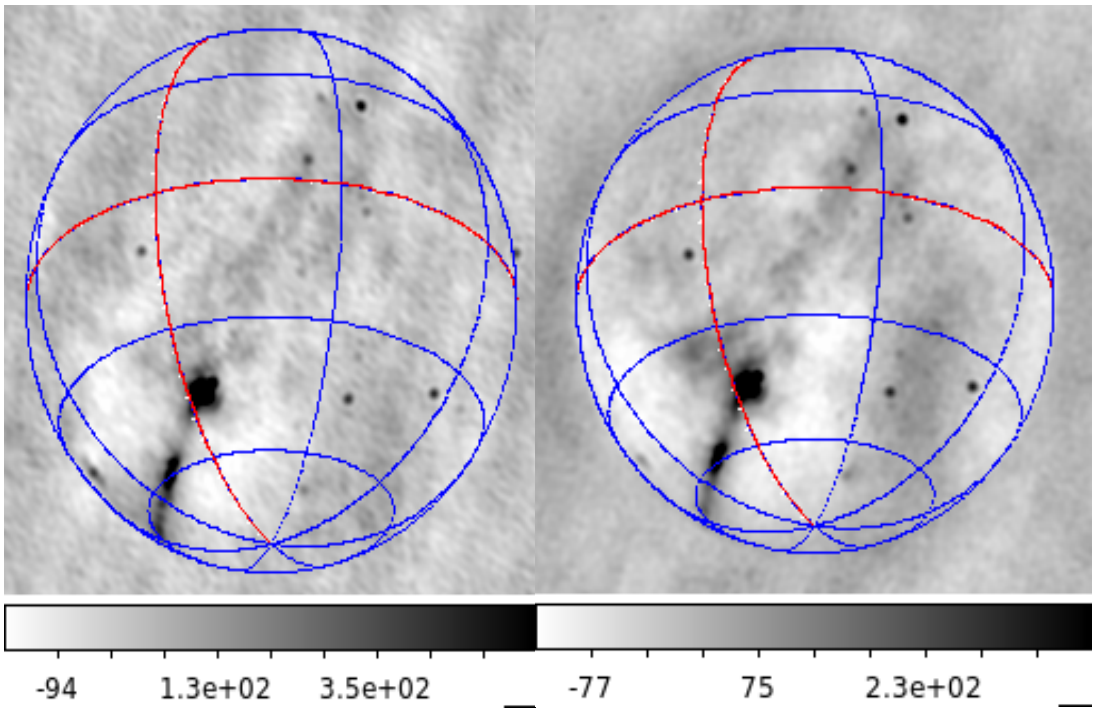

Figure 13: All-sky images at 230 MHz made from two seconds of data with a single polarization (North-South oriented antenna elements). Left: AAVS2.0, right: MWA Antenna. These images were generated using a calibration phase transfer from a solar observation approximately 6 hours prior. The slightly different resolution is due to the AAVS2.0 array being physically larger than MWA Antenna.

These types of all-sky images were also used to calculate station sensitivity as a function of local time, which was compared with the simulations [12]. These tests showed that the best agreement between the measured sensitivity and simulations was achieved at the time of the calibration (near the local midday). Therefore, alternative calibration methods using all-sky sky models, such as the so-called HASLAM map [15], were also tested in order to enable calibrating more often and correcting for the varying response of the instrument due to changing environmental factors (mainly ambient temperature). Moreover, these methods can be used over a wider range of local sidereal times (LSTs), including when the Sun is below horizon.

3.9 Considerations on calibration stability

In the framework of the AAVS2.0 sensitivity analysis (difference imaging technique), two different calibration approaches were applied, using the Sun as a point-like calibration source. In the first one (self-calibration), separate calibration solutions were calculated for each snapshot in which the Sun was above 45 degrees elevation. This limit was chosen to avoid angular regions outside the field of view of the array. In the second method (single snapshot calibration), only one snapshot close to the Sun transit was calibrated, and the calibration solutions were transferred to all the other snapshots over 24 hours. An example of the preliminary results of this analysis is shown in Figure 14 for the 160 MHz frequency channel in Y polarization. The observation was carried out on April 8th, 2020. In the common LST interval, the sensitivities derived using the two approaches are consistent with each other. This suggests that the system calibration is fairly stable over several hours. An inspection of the images obtained with the snapshot calibration during 24 hours indicates that the calibration stability persists over longer timescales.

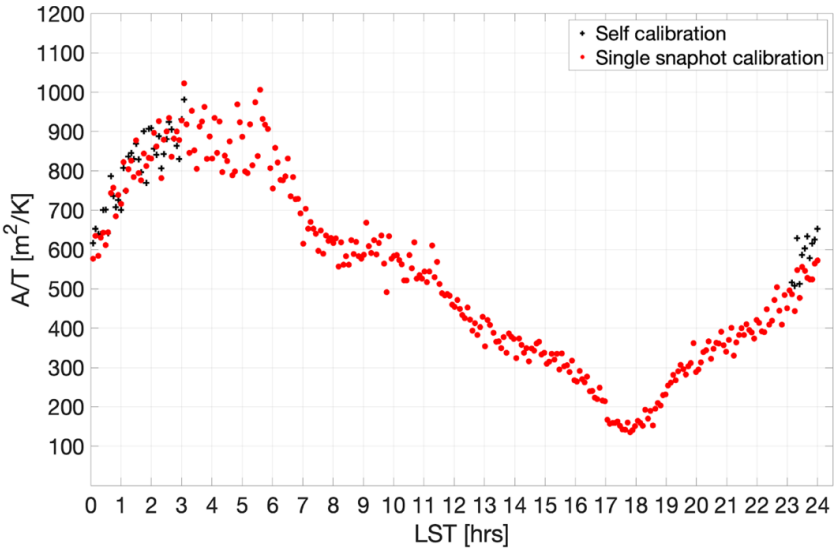

Figure 14: Channel 204 measured SKA1-Low sensitivity (in m^2K^{-1}), as a function of LST (in hour), Y polarization. Results from the two calibration methods are plotted with different marks (red dots for single snapshot calibration, black crosses for self-calibration).

3.10 Real-Time Station Beamforming

The default of the station beamforming is such that the real-time station beam is pointed at zenith, i.e. signals from all the antennas are coherently added at zenith. In order to verify the performance of the real-time station beamforming, the station beam was pointed at zenith and complex voltages were recorded over an interval of at least 24 hours, in a so-called drift scan mode. In the same time short (0.28 second) snapshots of voltages from all the antennas were recorded to compare the performance of the real-time beamforming against the off-line beamforming, and both were compared with the simulations, which was used as a main reference. For both data-sets (real-time and off-line beamformed data) the power (magnitude of

complex voltages) was plotted as a function of time and this kind of plots are referred to as a lightcurve. It was confirmed that the lightcurves resulting from the real-time beamforming were the same as those resulting from its off-line version, which validated the real-time beamforming procedure.

Furthermore, both lightcurves were compared with the predictions of a simulation using an array factor method of calculating the station power beam as described in [12]. The observed station beam power is expected to be proportional (by a factor corresponding to the system gain) to the system temperature T_{sys}, which is a sum of antenna temperature T_{ant} and receiver temperature T_{rcv} ($T_{sys} = T_{ant} + T_{rcv}$). Receiver temperature of the AAVS2.0 station was measured in the laboratory and was assumed to be approximately 40 K, whilst the antenna temperature can be calculated in the simulation as an integral of the sky brightness temperature (T_{sky}) weighted by the station beam power pattern, according to the following equation:

$$T_{ant} = \frac{\int_{4\pi} B_{st}(\nu,\theta,\phi) T_{sky}(\nu,\theta,\phi,t) d\Omega}{\int_{4\pi} B_{st}(\nu,\theta,\phi) d\Omega}$$

where T_{sky} is the sky temperature based on the so-called "HASLAM map" at 408 MHz [15] scaled down to the observing frequencies using a spectral index -2.5 [17]. The B_{st} is the station beam power pattern which was obtained from the aforementioned array factor simulation.

Figure 15 shows an example comparison between the simulation and data lightcurves from an approximately 36 hour long observation started at 2020-03-28 17:22 AWST with the real-time station beam pointed at zenith at the frequency 159.375 MHz. The data were normalised to the simulation at the maximum of the lightcurve and the normalisation factor N was calculated as $N = (T_{ant}^{model}(t_{gc}) + T_{rcv}) / P(t_{gc})$, where $T_{ant}^{model}(t_{gc})$ and $P(t_{gc})$ are the simulated antenna temperature and the observed station beam power at the time t_{gc} when Galactic Center was transiting overhead. In order to over-plot the data and simulations, all the data points were multiplied by the normalisation factor N and the resulting total power observed by the station is shown in units of dB.
The agreement between the data and simulation is very good and slightly better for the Y polarization, which agrees with similar differences also observed in sensitivity data. It was confirmed that the analogue signal chain is more stable for the Y polarization. The relatively small (below 1 dB) differences between the data and simulation can be attributed to a combination of small inaccuracies of the calibration coefficients and uncertainties of the sky model, which are of the order of 10 - 20%. Similar lightcurves were also generated from the observations at other frequencies with a good (within 2 dB) level of agreement between the data and simulations, confirming that the real-time beamforming is performing correctly.

The station beam can be electronically steered in an arbitrary direction in the sky, by applying additional phase corrections for each antenna and for each coarse channel. The off-zenith station beam steering was tested on different targets. Additionally, it was also verified by observations and regular detections of known bright pulsars, which will be reported in future publications.

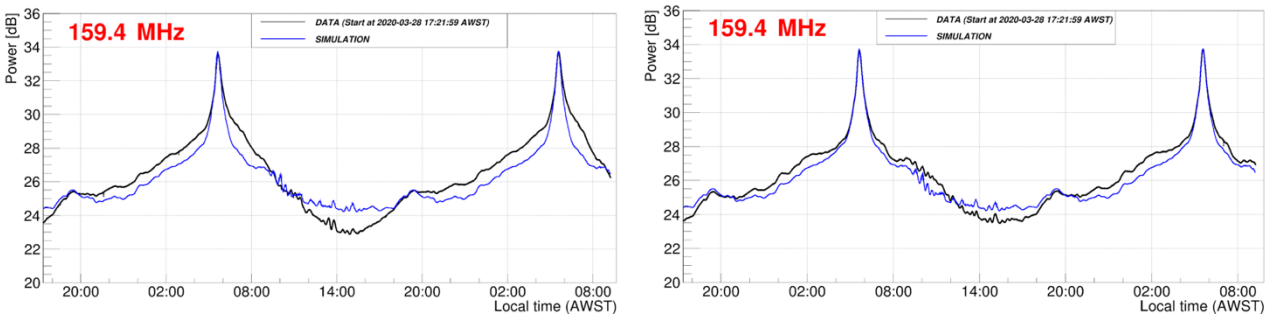

Figure 15: Power vs. time resulting from approximately 36 hours of observation with the real-time station beam pointed at zenith (so called drift scan mode). The data (black curves) are over-plotted with the simulation (blue curves). Left image shows X polarization and right image Y polarization. Some data points affected by radio-frequency interference were removed.

4 DISCUSSION AND FURTHER WORK

4.1 System CDR Recommendations

The work as presented here demonstrated that the AAVS2.0 prototype has addressed the high-level concerns of the LFAA CDR panel:

- The calibration effort shows good stability over longer periods of time and a calibration performance that is equal to the level of its predecessors [10].
- The real time beamforming is working as expected based on the comparison of the drift scans with the simulations. Although not shown here, the EM simulations permit in-depth analysis of beam pointing in all directions.
- The work on EM simulations have firstly shown that two independent EM simulations have a high level of agreement on the EM characteristics of the SKA-Low stations, and secondly that the UAV experiments show good agreement with the simulation results. The work performed here has significantly enhanced our understanding of the EEP's in practice.

Additionally, both the theoretical and experimental work has permitted verification of a large number of high-level SKA1 performance requirements such as station sensitivity and polarization purity, thereby significantly reducing the risk towards construction.

4.2 Future work

The short-term future work will consist of the following aspects:

1. So far only zenith pointing beams have been evaluated this will be extende with off-zenith beam pointing tests.
2. Performing a UAV test on the full stations, taking into account the lessons learned from the first test. The test will not be limited to verifying the EEP's but will also include station beamforming verification at a number of elevations
3. Further refinement of the distributed power and signal distribution network.

It is expected the AAVS2.0 prototype will remain in operation in 2021 and will be used for further tests on the different station hardware systems in the industrialisation phase for construction. The construction of the AA0.5, initially two full SKA-Low stations extended to 6, will start in early 2023; this will initially be a station production prototype that will later be extended to a system prototype, including inter-station calibration to permit verification of interferometric imaging on SKA-Low

REFERENCES

1. M.G. Labate, P. Dewdney, R. Braun, M. Waterson, J. Wagg (2017). "The SKA low-frequency telescope: Performance parameters and constraints on the array configuration". In 2017 11th European Conference on Antennas and Propagation (EUCAP) (pp. 2259–2263). Paris. https://doi.org/10.23919/EuCAP.2017.7928622
2. P. E. Dewdney, SKA Engineering team, "SKA1 Design Baseline Description", 2020, internal SKA document number SKA-TEL-SKO-0001075.
3. E. de Lera Acedo, H. Pienaar and N. Fagnoni, "Antenna design for the SKA1-LOW and HERA super radio telescopes," *2018 International Conference on Electromagnetics in Advanced Applications (ICEAA)*, Cartagena des Indias, 2018, pp. 636-639, doi: 10.1109/ICEAA.2018.8520395.
4. https://www.idscorporation.com/pf/galileo-suite/
5. P. Bolli, L. Mezzadrelli *et al.*, "Test-driven design of an active dual-polarized log-periodic antenna for the square kilometre array," IEEE Open Journal of Antennas and Propagation, vol. 1, pp. 253–263, 2020.
6. M. F. Waterson *et al.*, "Report on the Station Calibration Task", 2020, internal SKA document number, SKA-TEL-SKO-0001088.

7. D. B. Davidson, P. Bolli *et al*., "Electromagnetic modelling of the SKA-LOW AAVS1.5 prototype," *2019 International Conference on Electromagnetics in Advanced Applications (ICEAA)*, Granada, Spain, 2019, pp. 1032-1037, doi: 10.1109/ICEAA.2019.8879294.
8. D. B. Davidson, P. Bolli, et al, "Electromagnetic modelling of the SKA-LOW AAVS2 prototype," in 2020 XXXIIIrd General Assembly and Scientific Symposium of the International Union of Radio Science, Rome, Italy, 2020, pp. 1-4, doi: 10.23919/URSIGASS49373.2020.9232307.
9. P. Benthem, R. Wayth et al, ""The Aperture Array Verification System 1: System overview and early commissioning results" in preparation
10. F. Paonessa, L. Ciorba et al., "First Results on the Experimental Validation of the SKA-low Prototypes Deployed in Australia Using
11. Warnick, K. F., et al. "Phased arrays for radio astronomy, remote sensing, and satellite communications", Cambridge University Press, 2019.
12. M. Sokoloswki et al, "Preliminary verification of the SKA-Low AAVS2 prototype sensitivity", submitted to EUCAP 2021, to be held in Germany, April 2021.
13. Comoretto, G. et al., "The Signal Processing Firmware for the Low Frequency Aperture Array", Journal of Astronomical Instrumentation, Vol. 6, No. 1, Mar 2017
14. Naldi, G., et al., "The Digital Signal Processing Platform for the Low Frequency Aperture Array: Preliminary Results on the Data Acquisition Unit", Journal of Astronomical Instrumentation, Vol. 6, No. 1, Mar 2017
15. Haslam, C. G. T., Salter C. J., Stoffel H., Wilson W. E., "A 408 MHz all-sky continuum survey. II - The atlas of contour maps", Astronomy & Astrophysics, Supplement, Vol. 47, Jan 1982
16. "A retrospective view of *Miriad*", by Sault R.J., Teuben P.J., & Wright M.C.H., 1995. In *Astronomical Data Analysis Software and Systems IV*, ed. R. Shaw, H.E. Payne, J.J.E. Hayes, ASP Conference Series, **77**, 433-436
17. Mozdzen, T. J., et al., "Spectral index of the diffuse radio background between 50 and 100 MHz", MNRAS, Vol. 483, Mar 2019.
18. P. Bolli et al., "Antenna pattern characterization of the low-frequency receptor of LOFAR by means of an UAV-mounted artificial test source," SPIE Ground-based and Airborne Telescopes VI, Edinburgh, Scotland, United Kingdom, June 26 – July 1 2016. DOI 10.1117/12.2232419
19. E. de Lera Acedo et al., "SKA Aperture Array Verification System: Electromagnetic modeling and beam pattern measurements using a micro UAV", Experimental Astronomy, vol. 45, issue 1, pp. 1–20, Mar. 2018. DOI: 10.1007/s10686-017-9566-x
20. G. Pupillo et al., "Medicina Array Demonstrator: calibration and radiation pattern characterization using a UAV-mounted radio-frequency source," Experimental Astronomy, vol. 39, issue 2, pp. 405-421, June 2015. DOI: 10.1007/s10686-015-9456-z
21. P. Bolli et al., "From MAD to SAD: the Italian experience for the Low Frequency Aperture Array of SKA1-LOW", Radio Science, vol. 51, issue 3, pp. 160–175, Mar. 2016. DOI: 10.1002/2015RS005922
22. G. Virone et al., "Strong Mutual Coupling Effects on LOFAR: Modeling and In Situ Validation," IEEE Transactions on Antennas and Propagation, vol. 66, no. 5, pp. 2581-2588, May 2018. DOI: 10.1109/TAP.2018.2816651
23. P. Bolli et al., "Near-Field Experimental Verification of the EM Models for the LOFAR Radio Telescope," IEEE Antennas and Wireless Propagation Letters, vol. 17, issue 4, pp. 613–616, Apr. 2018. DOI: 10.1109/LAWP.2018.2859828
24. P. Di Ninni, P. Bolli, F. Paonessa, G. Pupillo, G. Virone, S. J. Wijnholds, "Electromagnetic Analysis and Experimental Validation of the LOFAR Radiation Patterns", International Journal of Antennas and Propagation, January 2019, doi:10.1155/2019/9191580
25. F. Paonessa, L. Ciorba, G. Virone, P. Bolli, A. Magro, A. McPhail, D. Minchin, and R. Bhushan, "SKA-low Prototypes Deployed in Australia: Synoptic of the UAV-based Experimental Results," Radio Science Letters, to be published
26. F. Paonessa, et al. "Differential phase patterns of the LOFAR LBA array measured in situ", 12th European Conference on Antennas and Propagation, London, UK, 9-13 April 2018
27. Benz, A., et al., "Radio Emission of the Quiet Sun", Landolt Bornstein, Vol. 4B, Jan 2019